

Received 00th January  
20xx,

## Tri-doped calcium fluoride based thin films for energy conversion: a comparison of MOCVD and sol-gel preparation methods

Anna L. Pellegrino,<sup>a</sup> Salvatore La Manna,<sup>a</sup> Ausrine Bartasyte,<sup>b</sup> Paolo Cortelletti,<sup>c</sup> Giacomo Lucchini,<sup>c</sup> Adolfo Speghini<sup>c,\*</sup> and Graziella Malandrino<sup>a,\*</sup>

Accepted 00th January 20xx

DOI: 10.1039/x0xx00000x

www.rsc.org/

Starting from fluorinated metalorganic  $\beta$ -diketonates we report the synthesis of undoped and lanthanide-doped alkaline-earth fluoride ( $\text{Er}^{3+}, \text{Tm}^{3+}, \text{Yb}^{3+}$  tri-doped  $\text{CaF}_2$ ) thin films through two different chemical approaches: Metal-Organic Chemical Vapor Deposition (MOCVD) and a combined sol-gel/spin-coating procedure. Both chemical approaches have the advantage of being very reliable and reproducible for the fast production of thin films with high uniformity degree over large areas. The fluorinated metal precursors act as a single-source in both processes, and an accurate control of the process parameters allows the optimization of the doped  $\text{CaF}_2$  films. X-ray diffraction, field emission scanning electron microscopy and energy dispersive X-ray analysis have been used to characterize the deposited films. Upconversion emission, typical of the lanthanide ions, in the visible and near infrared regions upon laser excitation at 980 nm are clearly observable. The emissions are in the central region of the CIE1931 color coordinate space.

### Introduction

Fluoride based materials are nowadays among the most promising inorganic functional systems for a wide variety of applications in dielectrics, optics, optoelectronics, and photonics.<sup>1</sup> In particular, lanthanide doped binary or multicomponent fluorides are nowadays extensively investigated for their excellent chemical and optical properties, which find applications in microelectronics and photonics, as well as nanomedicine, both in massive and also in nanostructured forms.<sup>2</sup>

In recent years, the exponential growth of research activities in the production of new and more efficient photovoltaic (PV) devices has boosted the research activity towards the fabrication of fluoride materials in thin film form as energy converting layers.<sup>3</sup> In fact, one interesting strategy to enhance the efficiency of PV devices is to collect the solar radiation outside of the absorption range of the photoactive material (e.g. silicon) and to shift its energy to a more suitable optical region, i.e. the visible range, in which it can be efficiently harvested by the PV device. To this aim, trivalent lanthanide ions ( $\text{Ln}^{3+}$ ) doped fluorides have been considered among the

most effective materials for energy conversion processes.<sup>4</sup> In particular, properly lanthanide ions doped (e.g. ytterbium/erbium,  $\text{Yb}^{3+}/\text{Er}^{3+}$ , or ytterbium/thulium,  $\text{Yb}^{3+}/\text{Tm}^{3+}$ ) binary (e.g.  $\text{CaF}_2$  or  $\text{SrF}_2$ ) and ternary ( $\text{NaYF}_4$ ,<sup>5</sup>  $\text{NaGdF}_4$ ,<sup>2f,6</sup> or  $\text{LiYF}_4$ ,<sup>7</sup>) fluorides have been demonstrated very efficient hosts for energy down-conversion or upconversion processes (UC). UC is a process in which two or more photons, typically in the near infrared region (NIR), are converted into photons with higher energy, usually in the visible or ultraviolet (UV) regions. The so-called Energy Transfer Upconversion (ETU) process, typical of lanthanide doped inorganic materials, is efficiently able to generate strong UC emissions in the visible and UV regions upon NIR excitation, usually close to 1  $\mu\text{m}$ . The UC mechanism involves sensitizers, such as  $\text{Yb}^{3+}$  ions, that efficiently absorb photons in the NIR region around 980 nm and transfer energy to activator ions, such as  $\text{Er}^{3+}$ ,  $\text{Tm}^{3+}$  or  $\text{Ho}^{3+}$ , in several steps thanks to the peculiar ladder-like energy level scheme of the  $\text{Ln}^{3+}$  ions, in order to obtain photons with higher energy.<sup>8</sup>  $\text{Ln}^{3+}$  codoped fluoride materials are also of paramount interest as inorganic phosphors for producing white light emission through mixing of red, green and blue emissions due to  $\text{Er}^{3+}$  and  $\text{Tm}^{3+}$  ions in appropriate proportions. These systems have the advantages of being cheap, showing efficient luminescence and, if available through an easy synthetic route, also appealing for the industrial production.<sup>2c,9</sup> Interestingly,  $\text{Ln}^{3+}$  doped fluoride compounds in thin film form show promising luminescent properties in microelectronic applications as micro- and nanoscale thermometry, due to the tight correlation between temperature and luminescent behavior of emitting doping ions.<sup>10</sup>

<sup>a</sup> Dipartimento di Scienze Chimiche, Università di Catania and INSTM UdR Catania, V.le A. Doria 6, 95125 Catania, Italy. E-mail: gmalandrino@unicat.it

<sup>b</sup> FEMTO-ST Institute, University Franche-Comté, 26 rue de l'Épitaphe, Besançon 25030, France

<sup>c</sup> Nanomaterials Research Group, Dipartimento di Biotecnologie, Università di Verona and INSTM, UdR Verona, Strada Le Grazie 15, I-37134 Verona, Italy. Email: aspeghini@univr.it

† Electronic Supplementary Information (ESI) available: [Reactor scheme, EDX spectra, XRD pattern]. See DOI: 10.1039/x0xx00000x

Among binary fluorides, calcium fluoride has been regarded as one of the most efficient host for  $\text{Ln}^{3+}$  luminescent ions for energy conversion systems, due to its low phonon energies, which minimizes non-radiative de-excitation processes.<sup>11</sup> Some investigations have been reported in the literature on doped  $\text{CaF}_2$  nanoparticles for applications in nanomedicine,<sup>2b,2e</sup> while differently  $\text{Ln}^{3+}$  doped  $\text{CaF}_2$  thin films have been much less investigated. Specifically,  $\text{CaF}_2$  thin layers have been grown through physical vapor deposition techniques,<sup>12</sup> such as electron beam evaporation<sup>13</sup> and molecular beam epitaxy.<sup>14</sup> Nonetheless, few reports are known on chemical deposition techniques either solution or vapor phase routes.<sup>15,16</sup> Ternary fluorides such as  $\text{NaYF}_4$  and  $\text{NaGdF}_4$ , deeply studied as nanoparticles,<sup>17</sup> have been also recently investigated in thin film forms.<sup>18,19</sup>

In the present paper, an in-depth study is reported describing the MOCVD and sol-gel approaches for the fabrication of binary fluoride  $\text{CaF}_2$  thin films, also doped with lanthanide ions. The two methods are compared by using the same  $\beta$ -diketonate precursor for the formation of the  $\text{CaF}_2$  phase, namely the fluorinated "second-generation"  $\text{Ca}(\text{hfa})_2 \cdot \text{diglyme} \cdot \text{H}_2\text{O}$ . After the sol-gel procedure, the spin-coating deposition has been applied for the formation of compact thin films. Lanthanide tri-doped systems, namely  $\text{CaF}_2:\text{Yb}^{3+}, \text{Er}^{3+}, \text{Tm}^{3+}$  have been obtained by MOCVD and sol-gel/spin-coating methods, through simple and easily scalable processes adding the analogous  $\text{Ln}(\text{hfa})_3 \cdot \text{diglyme}$  ( $\text{Ln} = \text{Yb}, \text{Er}, \text{Tm}$ ) adducts as doping agents in the precursor sources.

X-ray diffraction (XRD), field-emission scanning electron microscopy (FE-SEM) and energy dispersive X-ray (EDX) analyses allowed an accurate determination of the physico-chemical properties of deposited layers, while their functional properties were assessed through luminescence spectroscopy.

## Experimental

**Film syntheses.** All the precursors have been synthesized as previously reported in ref. 20-21.

MOCVD depositions take place in a horizontal hot-wall reactor (Fig. S1, ESI<sup>†</sup>), under low-pressure using argon as carrier gas and oxygen as the reactant gas, which was introduced in the main flow in proximity to the reaction zone. The films were deposited on Si(001), glass and quartz in the 400-550 °C temperature range. The molten precursor source of doped  $\text{CaF}_2$  was heated at 120 °C, which is a useful temperature for an efficient vaporization.

The sol-gel reaction occurred in water/ethanol solution with trifluoroacetic acid ( $\text{CF}_3\text{COOH}$ ) as catalyst for the hydrolysis reactions. The sol was aged at 60 °C for 20h and spin-coated on Si(001) and glass substrates. The spin-coating process was carried out using a multistep procedure in which four times of spin-coating deposition are alternated to fast annealing steps at 350 °C or 400 °C in air for 10 min. Finally, the films were annealed at 350 °C or 400 °C in air for 1 h. A Spin-Coater SPIN-

150 SPS Europe has been used at speed rate of 1000 RPM/sec, 3000 round per minute (RPM) and time of 60s.

**Film characterizations.** Film structure was analyzed by XRD using a Smartlab Rigaku diffractometer in grazing incidence mode (0.5°), equipped with a rotating anode of  $\text{Cu K}\alpha$  radiation operating at 45 kV and 200 mA. Film surface morphology was investigated using the field emission scanning electron microscopy (FE-SEM) ZEISS SUPRA 55 VP. The films deposited on glass were Au-coated prior FE-SEM characterization. The atomic composition of the samples was performed through energy dispersive X-Ray (EDX) analysis, using an INCA-Oxford windowless detector, having a resolution of 127 eV as the FWHM of the  $\text{Mn K}\alpha$ .

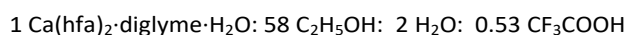
**Upconversion emission measurements.** A 980 nm diode laser (CNI Optoelectronics Tech) was used as an excitation source to generate UC emission. For measuring the decay curves, an Arduino hardware platform and proper software were used to modulate the 980 nm laser, generating a 10 Hz wave with a decay time of 1  $\mu\text{s}$ . The emission spectra were recorded using a half meter monochromator (Andor, Shamrock 500i) equipped with a 300 lines/mm grating and an iDus CCD camera. The emission signal was collected with a 40x microscopy objective (Nikon, Plan Fluor) using a dichroic mirror (Semrock, 925 nm edge BrightLine beamsplitter). The decay curves were acquired with a GaAs photomultiplier (Hamamatsu) and a 500 MHz Oscilloscope (LeCroy, Waverunner).

## Results and discussion

Vapor phase and solution routes have been implemented for the deposition of calcium fluoride thin films applying the same precursors of the type  $\text{M}(\text{hfa})_n \cdot \text{diglyme}$ . These complexes act as single-source precursors for all the required elements Ca, Ln ( $\text{Ln} = \text{Yb}, \text{Er}, \text{Tm}$ ) and fluorine in both processes. Undoped  $\text{CaF}_2$  films and tri-doped  $\text{CaF}_2:\text{Yb}^{3+}, \text{Er}^{3+}, \text{Tm}^{3+}$  ones have been deposited through MOCVD and sol-gel/spin-coating approaches. To assess reproducibility of the used approach, each experiment, either through sol-gel or MOCVD, has been repeated two or three times.

### Fabrication of binary fluoride $\text{CaF}_2$ and $\text{Ln}^{3+}$ tri-doped $\text{CaF}_2$ films through a sol-gel/spin-coating approach

The  $\text{Ca}(\text{hfa})_2 \cdot \text{diglyme} \cdot \text{H}_2\text{O}$  adduct has been applied in a sol-gel approach under acidic condition with the following reagent molar ratio:



The sol is heat treated at 60 °C for 20 h to produce an incipient gel which may be spun to yield  $\text{CaF}_2$  films through iterative spinning and thermal treatment both on Si and glass substrates. The final annealing temperature was 350 °C or 400 °C.

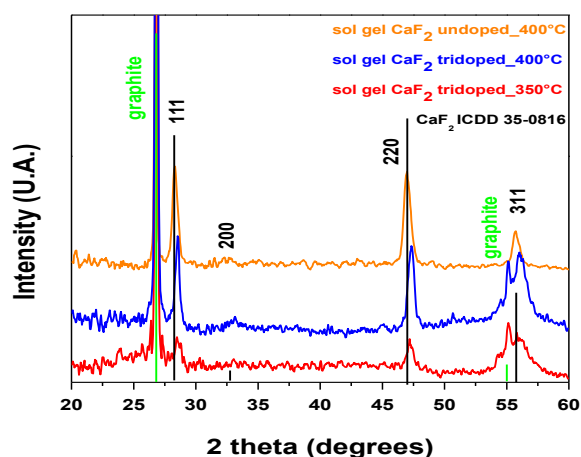
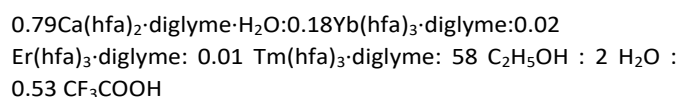


**Fig. 1** XRD patterns of sol-gel/spin-coated films on Si (100): undoped  $\text{CaF}_2$  film (400 °C, orange line),  $\text{CaF}_2\text{:Yb}^{3+},\text{Er}^{3+},\text{Tm}^{3+}$  (350 °C, red line), and  $\text{CaF}_2\text{:Yb}^{3+},\text{Er}^{3+},\text{Tm}^{3+}$  film (400 °C, blue line). Graphite reflections are indicated as green lines.

The same procedure has been applied to the preparation of tri-doped  $\text{CaF}_2\text{:Yb}(18\%),\text{Er}(2\%),\text{Tm}(1\%)$  thin films using  $\text{Yb}(\text{hfa})_3\cdot\text{diglyme}$ ,  $\text{Er}(\text{hfa})_3\cdot\text{diglyme}$  and  $\text{Tm}(\text{hfa})_3\cdot\text{diglyme}$  as Yb, Er and Tm sources respectively, by means of the following reagent molar ratio:



The X-ray diffraction (XRD) analyses, performed on the films obtained on both Si and glass, show diffraction patterns with features attributable to the pure  $\text{CaF}_2$  phase, confirming its formation for all the samples independently on the substrate nature (see Fig. S2, ESI<sup>†</sup>). In Fig. 1 the XRD patterns of undoped  $\text{CaF}_2$  film, annealed at 400 °C (orange pattern), and  $\text{CaF}_2\text{:Yb}(18\%),\text{Er}(2\%),\text{Tm}(1\%)$  samples annealed at 350 °C (red pattern) and 400 °C (blue pattern) show characteristic peaks at  $2\theta=28.25^\circ, 47.00^\circ, 55.75^\circ$  corresponding to reflections of the (111), (220), (311) lattice planes, respectively, typical of the  $\text{CaF}_2$  phase (ICDD diffraction card 35-0816).

The observed peak intensities match exactly those reported in the ICDD card, thus indicating the formation of polycrystalline films without any preferential orientation. It is interesting to observe that the tri-doped sample treated at 350 °C (red pattern, Fig. 1) shows a lower crystallinity degree, while the sample treated at 400 °C (blue pattern, Fig. 1) is more crystalline as indicated by the higher intensities of the peaks. The internal graphite standard has allowed to assess that the diffraction peaks of the tri-doped  $\text{Ln}^{3+}$  samples are shifted towards higher angles than for the undoped  $\text{CaF}_2$ , indicating a smaller  $a$ -axis parameter (see Table S1, ESI<sup>†</sup>). This behaviour clearly demonstrate that the dopant lanthanide ions are incorporated in the crystal host (see also the results for samples prepared by MOCVD technique). Moreover, the absence of other peaks in the patterns suggests the exclusive formation of the phase of interest.

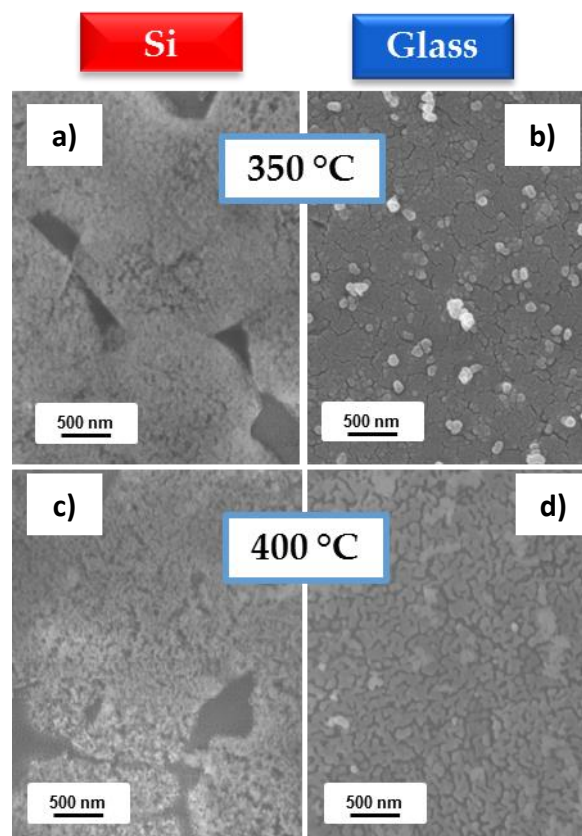


**Fig. 2** FE-SEM images of sol-gel/spin-coated pure  $\text{CaF}_2$  film annealed at 350 °C and 400 °C on Si (a,c) and glass (b,d).

The field emission scanning electron microscopy (FE-SEM) images in Fig. 2 of the pure  $\text{CaF}_2$  films obtained on Si and glass substrates, under the same deposition conditions (annealing at 350 °C and 400 °C), show different morphologies. Samples deposited on Si (Fig. 2a, 2c) show quite homogeneous surfaces, even though the surface presents some shrinkage due to the annealing temperature. In contrast, the samples deposited on glass in Fig. 2b and 2d show the formation of more homogeneous coatings with small grains of the order of about 150-200 nm, and the presence of barely visible cracks. For tri-doped films treated at 350 °C or 400 °C, the EDX analysis has yielded a stoichiometry for the layer of 0.80 Ca: 0.18 Yb (Fig. S3). Erbium and thulium elements are not detected, being their amounts under the detectability limit of the technique. On the other hand, their presence has been undoubtedly confirmed by their spectroscopy properties, as described below. The FE-SEM images of the tri-doped films deposited on Si at 350 and 400 °C show a quite homogeneous morphology (Fig. 3a and 3b, respectively), similar to the undoped ones, with grains of about 50 nm. The FE-SEM cross-section images (Fig. 3c and 3d) show a thickness of about  $700 \pm 35$  nm and  $750 \pm 45$  nm for the films treated at 350 °C and 400 °C, respectively. From these characterizations, it can be stated that the two different temperatures adopted for the thermal treatment do not significantly affect either the morphology or the phase nature, but only the crystalline characteristics of the layer, fixing the minimum temperature

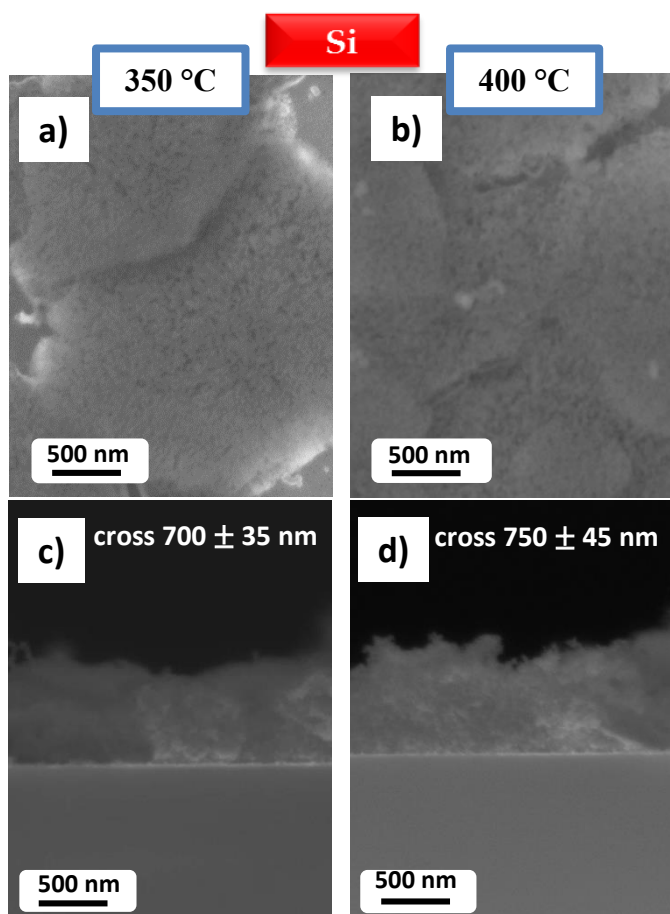


Fig. 3 FE-SEM plan view and cross-section images of sol-gel/spin-coated tri-doped  $\text{CaF}_2$  film on Si annealed at 350 °C (a,c) and 400 °C (b,d).

to reach the crystalline  $\text{CaF}_2$  phase at 350 °C under these experimental conditions.

In addition, all samples show the formation of single phase  $\text{CaF}_2$ , as assessed by XRD, on both the two different substrates. Conversely, the substrate nature seems to play an important role in film homogeneity, indicated by a lower homogeneity for films deposited on Si with respect to those deposited on glass. This may be likely due to the different wettability of untreated Si and glass substrates. In addition, the cracking and the shrinkage may be due to the thermal treatment after spin-coating, which is a well-known phenomenon in sol-gel prepared samples.<sup>22</sup>

The properties of these films are comparable to those previously reported for the unique example of sol-gel grown pure  $\text{CaF}_2$  films on glass substrates.<sup>23</sup> Nevertheless, it is worth to note that present samples are obtained at treatment temperatures that are 100–150 °C lower than those previously reported.<sup>23</sup>

#### Fabrication of undoped and $\text{Ln}^{3+}$ tri-doped $\text{CaF}_2$ films through MOCVD approach

MOCVD has been successfully applied to the deposition of the  $\text{CaF}_2$  phase using the same  $\text{Ca}(\text{hfa})_2 \cdot \text{diglyme} \cdot \text{H}_2\text{O}$  adduct. Preliminary depositions using only the Ca precursor indicate

that the films are crystalline, pure  $\text{CaF}_2$  phase, compact and homogeneous on the whole area 10 x 10 mm<sup>2</sup>. One of the crucial issues in the fabrication of doped layers is to accurately tailor the composition of the deposited layer and to monitor the relationship of the film composition and precursor mixture stoichiometry.

Dynamic thermogravimetric (TG) measurements of the required single metal precursors and of a multicomponent mixture containing the main component Ca and Yb adducts in a 0.80:0.20 ratio have shown a good thermal behavior proper for application in an MOCVD process (Fig. 4). In particular, the TG curve of the Ca adduct shows a single step weight loss with a very low residue of about 1.8%. Similarly, the  $\text{Yb}(\text{hfa})_3 \cdot \text{diglyme}$ ,  $\text{Tm}(\text{hfa})_3 \cdot \text{diglyme}$  and  $\text{Er}(\text{hfa})_3 \cdot \text{diglyme}$  curves show a single step loss with a residue of about 2%. The TG curve of the Ca-Yb precursor mixture, indicates that the mixture behaves as a “single-source” precursor with a single step loss and a residue of 2%.

Thus, specific depositions were designed to assess the relationship between the precursor mixture ratios and the composition of the layers, with the aim to properly prepare suited lanthanide doped films for efficient UC emission, in particular with a lanthanide molar ratio Yb:Er:Tm of 0.18:0.02:0.01. This concentration doping represents one of the best ratios to achieve good upconversion properties.<sup>2f</sup>

Since small percentages of  $\text{Er}^{3+}$  and  $\text{Tm}^{3+}$  ions are difficult to be quantified with the usual analytical techniques employed for thin films, depositions with higher  $\text{Er}^{3+}$  and  $\text{Tm}^{3+}$  percentages have been carried out, in particular with a precursor molar metal ratio Ca:Yb:Er:Tm of 0.70:0.10:0.10:0.10. The correlation between the starting lanthanide molar percentages (indicated with red lines) and the actual percentages assessed through EDX, for  $\text{Yb}^{3+}$ ,  $\text{Er}^{3+}$  and  $\text{Tm}^{3+}$  ions, is reported in Fig. 5, while a typical EDX spectrum is reported in Fig. S4 (ESI<sup>†</sup>).

The three graphs shown in Fig. 5 indicate the distribution (as atomic percentage obtained through EDX) of each element, namely Yb, Er and Tm, for the two different positions A and B in the hot-wall reactor (A and B positions are indicated in the reactor scheme reported in Fig. S1 ESI<sup>†</sup>).

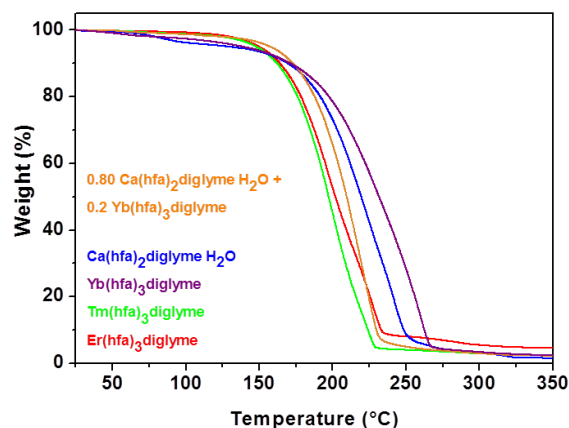


Fig. 4 Comparison of thermogravimetric curves of the single precursors,  $\text{Ca}(\text{hfa})_2 \cdot \text{diglyme} \cdot \text{H}_2\text{O}$  and  $\text{Ln}(\text{hfa})_3 \cdot \text{diglyme}$  ( $\text{Ln} = \text{Yb}, \text{Er}, \text{Tm}$ ), and of the  $\text{Ca}(\text{hfa})_2 \cdot \text{diglyme} \cdot \text{H}_2\text{O}$  and  $\text{Yb}(\text{hfa})_3 \cdot \text{diglyme}$  mixture in a Ca:Yb mole ratio of 0.80:0.20 (the main component of the  $\text{CaF}_2$ :  $\text{Yb}^{3+}$ ,  $\text{Er}^{3+}$ ,  $\text{Tm}^{3+}$  films).



**Table 1.** Deposition temperatures for thin films samples prepared by MOCVD (compare with Fig 5).

Deposition	$T_{\text{nom}}$ (°C)	$T_{\text{dep}}$ (°C) (pos. A)	$T_{\text{dep}}$ (°C) (pos. B)
1	550	450 <b>1A</b>	500 <b>1B</b>
2	600	500 <b>2A</b>	550 <b>2B</b>
3	500	400 <b>3A</b>	450 <b>3B</b>

For a given nominal deposition temperature, **A** and **B** positions have 50 °C and 100 °C lower temperatures with respect to the nominal one, respectively. In Table 1 the legend of the sample names shown in Fig. 5 is reported.

All the temperatures reported in the following refer to the real deposition temperature based on the sample position (see Fig.

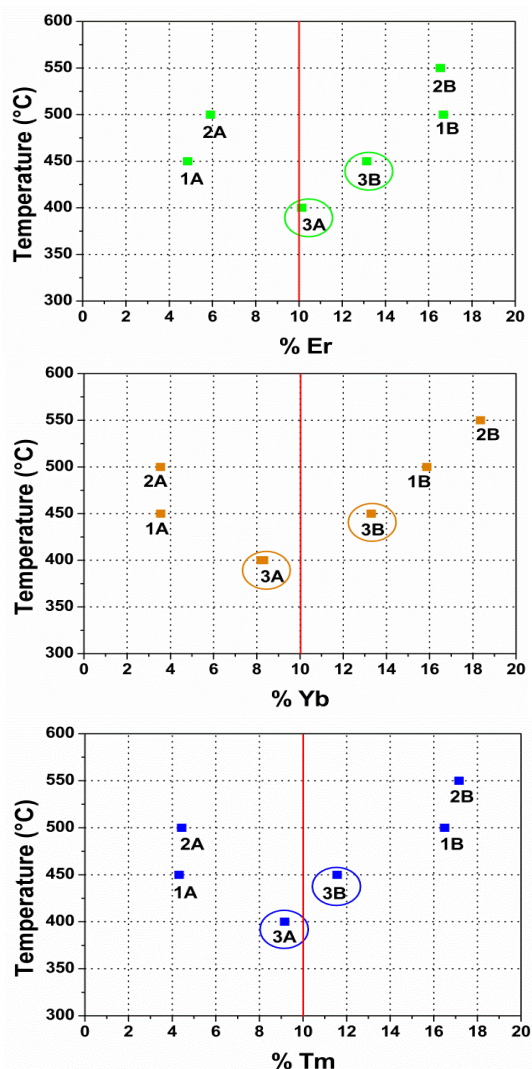


**Fig. 5** Yb, Er and Tm percentages in  $\text{CaF}_2$  doped films determined through EDX analysis vs deposition temperatures. The concentration of the doping ions in the precursors is 10% (red line) in all cases.

S1 ESIT). At a deposition temperature of 400 °C (**A** position) the metal atomic ratio of the samples result to be practically identical to the nominal one, while for the samples in the **B** position (at 450 °C) a slightly higher amount is found. At higher nominal temperatures, lower amounts are found at the **A** position, while higher amounts are found in **B** samples with respect to nominal composition. These trends can be rationalized by hypothesizing a different decomposition rate of the precursors, with the Ca precursor decomposing faster than the analogous lanthanide ones. Specifically, it is likely that in position **A**, therefore at lower temperature of the substrate, the calcium precursor deposits in greater amount with respect to the doping lanthanides, resulting in a net lower percentage of dopants in the final film. On the contrary, in position **B**, i.e. at higher temperatures, the vapor precursor mixture is richer in dopants than in calcium (already partially consumed in **A**), resulting in a net higher percentage of doping lanthanide ions. Therefore, the multicomponent mixture shows appropriate thermal behavior for its application in MOCVD processes, allowing an easy control of the film composition by tailoring the stoichiometric ratio of the multicomponent precursor mixture in function of the desired deposition temperature. It is worth to note that the use of the same polyether (diglyme), to complete the coordination sphere of calcium and lanthanide ions, avoids any possible ligand exchange.

The X-ray diffraction patterns of the undoped  $\text{CaF}_2$  films deposited by MOCVD in the 400-550 °C range do not show any difference either as a function of the temperature or the substrate nature, analogously to what found for the sol-gel/spin-coated films. It is instead interesting to notice the difference due to the lanthanide doping both in terms of peak positions and intensities. For a similar system, it has been previously observed,<sup>24</sup> that upon doping with Yb, Er or Yb, Tm, the peaks shift to higher 2 theta angles up to around 18% of  $\text{Yb}^{3+}$  doping concentrations. This corresponds to a decrease of the  $a$ -axis parameter for the doped film with respect to the undoped sample, while the 23% doped sample shows the same  $a$ -axis parameter of the 18% ytterbium doped  $\text{CaF}_2$  (see Table S1, ESIT).<sup>24</sup>

In Fig. 6, the XRD patterns of the  $\text{Ln}^{3+}$  tridoped 3A and 3B (see Table 1 and Fig. 5)  $\text{CaF}_2$  films (Ca:Yb:Er:Tm ratio of 0.70:0.10:0.10:0.10) prepared at two different temperatures are reported in comparison with a typical pattern of an undoped  $\text{CaF}_2$  film deposited at 450 °C. In the case of the tri-doped films, with an actual total  $\text{Ln}^{3+}$  (Yb+Er+Tm) concentration of 28% (3A sample) and 38% (3B sample), the  $a$ -axis cell parameter is equal to 5.47(6) Å and 5.47(7) Å, respectively. These concentrations have been estimated by the EDX results reported in Fig. 5, while the  $a$ -axis cell parameters have been estimated using graphite as an internal standard and by using the relationship between  $hkl$  and the lattice parameter for a cubic structure. The  $a$ -axis values for the tri-doped systems are larger than that obtained for the undoped  $\text{CaF}_2$  film, which results to be 5.46(0) Å. The  $a$ -axis cell parameters for undoped and tri-doped samples are reported in Table S1 (ESIT).

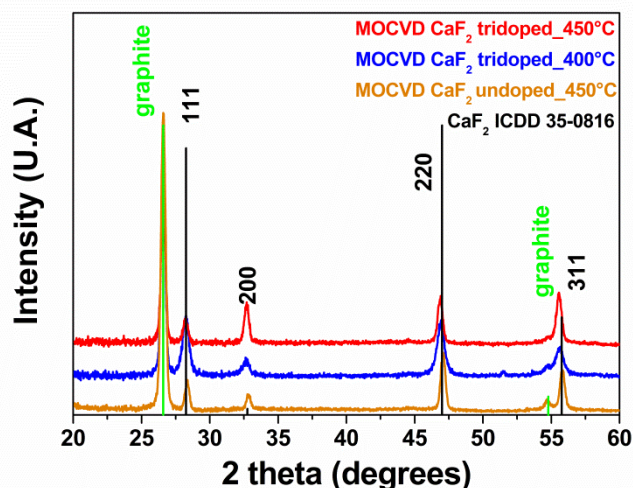


Fig. 6 X-ray diffraction patterns of the undoped and tri-doped 3A and 3B  $\text{CaF}_2:\text{Yb}^{3+}(10\%):\text{Er}^{3+}(10\%):\text{Tm}^{3+}(10\%)$  thin films prepared by MOCVD on Si substrate.

Two contributions may be considered for the  $a$ -axis parameter variation in the doped samples with respect to the undoped one: i) the difference of the ionic radii of the metal ions and ii) the effect of the charge compensation. The first contribution, i.e. the slight smaller ionic radius of  $\text{Ln}^{3+}$  vs.  $\text{Ca}^{2+}$  ( $\text{Yb}^{3+}$  ( $r = 0.985 \text{ \AA}$ ),  $\text{Er}^{3+}$  ( $r = 1.004 \text{ \AA}$ ),  $\text{Tm}^{3+}$  ( $r = 0.994 \text{ \AA}$ ),  $\text{Ca}^{2+}$  ( $r = 1.12 \text{ \AA}$ ) in eightfold coordination) is responsible for the decrease of the  $a$ -axis parameter, but this effect may be compensated by the second one, which is the insertion of interstitial fluoride ions or clusters, needed to balance the system charge. Thus, at this high ( $\approx 30\%$ ) doping, it is likely that the amount of fluoride ions or clusters to balance the charge is so substantial, that not only compensates the effect of the smaller lanthanide ionic radii but produces even larger  $a$ -values. A similar trend has been previously reported for highly doped  $\text{CaF}_2$  nanoparticles.<sup>25</sup>

In addition, it is interesting to observe that the relative intensities of peaks do not match very well those reported in the ICDD database. In particular, for the sample deposited at  $450 \text{ }^\circ\text{C}$  the 311 reflection is the most intense peak, while it has only a 33% intensity in the ICDD card, and the 200 peak is the second intense peak, while it is only around 1% in the ICDD card. This may be rationalized considering that the  $\text{Ln}^{3+}$  ions substitute  $\text{Ca}^{2+}$  ones and, being heavier, have larger scattering factors, thus producing a change of the peak relative intensities. Thus, if on one side the amount of doping ions plays a role on the relative peak intensities, since the intensity variation parallels the doping increasing, on the other hand, some preferential orientation may not be ruled out considering that also in the undoped  $\text{CaF}_2$  films the relative intensities do not perfectly match the ICDD card values.

The FE-SEM images (Fig. 7) show the morphology of the  $\text{CaF}_2:\text{Yb}^{3+}(10\%):\text{Er}^{3+}(10\%):\text{Tm}^{3+}(10\%)$  films on Si and glass substrates. All the samples present a very homogeneous surfaces with similar grains in form and dimensions. The films deposited at lower temperature, independently on the substrate nature, have very small grains coalesced to form large aggregates of hundreds of nm.

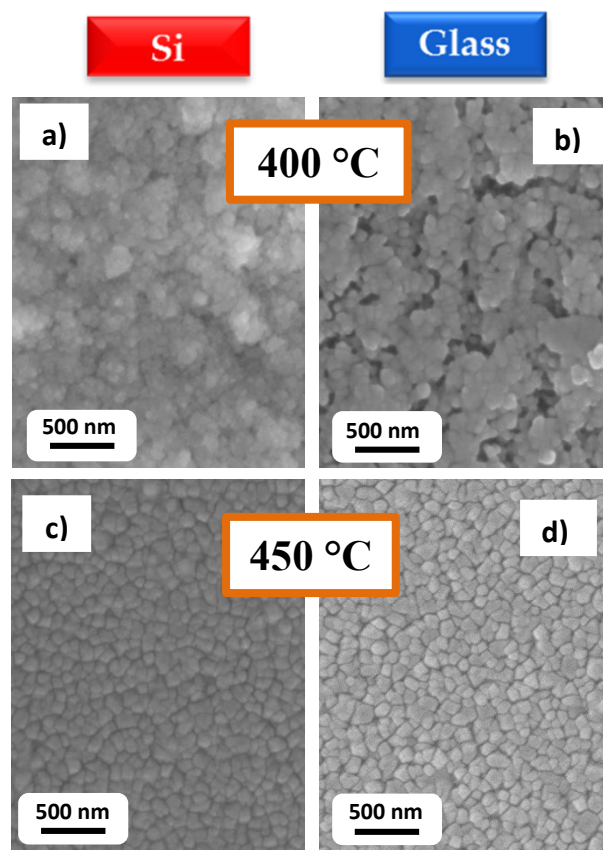


Fig. 7 FE-SEM images of  $\text{CaF}_2:\text{Yb}(10\%):\text{Er}(10\%):\text{Tm}(10\%)$  films prepared by MOCVD on Si substrate at  $400 \text{ }^\circ\text{C}$  (a) and  $450 \text{ }^\circ\text{C}$  (c) and on glass at  $400 \text{ }^\circ\text{C}$  (b) and  $450 \text{ }^\circ\text{C}$  (d).

At  $450 \text{ }^\circ\text{C}$ , films deposited on Si and glass show similar morphologies with single grains of about  $100 \text{ nm}$ . From these images, it can be stated that the two substrates used do not significantly affect the final morphology of the films at higher deposition temperature.

Taking into account all these results, we adopted the best experimental conditions for the deposition at  $400 \text{ }^\circ\text{C}$  and  $450 \text{ }^\circ\text{C}$  of tri-doped Yb, Er and Tm  $\text{CaF}_2$  films on Si and glass substrates, using a source mixture atomic ratio  $\text{Ca}:\text{Yb}:\text{Er}:\text{Tm}$  of  $0.80:0.18:0.02:0.01$ , denoted as  $\text{CaF}_2:\text{Yb}^{3+}(18\%):\text{Er}^{3+}(2\%):\text{Tm}^{3+}(1\%)$ . The EDX analysis confirmed that the films have a  $\text{Ca}:\text{Yb}$  stoichiometry of  $0.79:0.18$  (see Fig. S5, ESI<sup>†</sup>). Analogously to what observed for sol-gel/spin-coated tri-doped samples, the erbium and thulium elements are not detected by EDX. The FE-SEM images of the  $\text{CaF}_2:\text{Yb}^{3+}(18\%):\text{Er}^{3+}(2\%):\text{Tm}^{3+}(1\%)$  films are reported in Fig. 8. The morphologies are comparable to those obtained for the highly doped systems, whose morphologies are reported in Fig. 7. This implies that the morphologies are mainly affected by the deposition temperature and substrate nature and not by the lanthanide doping amount. The cross-section images of the  $\text{CaF}_2:\text{Yb}^{3+}(18\%):\text{Er}^{3+}(2\%):\text{Tm}^{3+}(1\%)$  films deposited on Si at  $400 \text{ }^\circ\text{C}$  and  $450 \text{ }^\circ\text{C}$  (whose plan views are shown in Fig. 8a and 8b, respectively) are reported in Fig. S6 (ESI<sup>†</sup>). The cross-sections indicate a thickness of about  $980 \pm 23 \text{ nm}$  and  $780 \pm 18 \text{ nm}$  respectively for the films deposited at  $400$  and  $450 \text{ }^\circ\text{C}$ , for an average growth rate of about  $1 \text{ } \mu\text{m}/\text{h}$ .

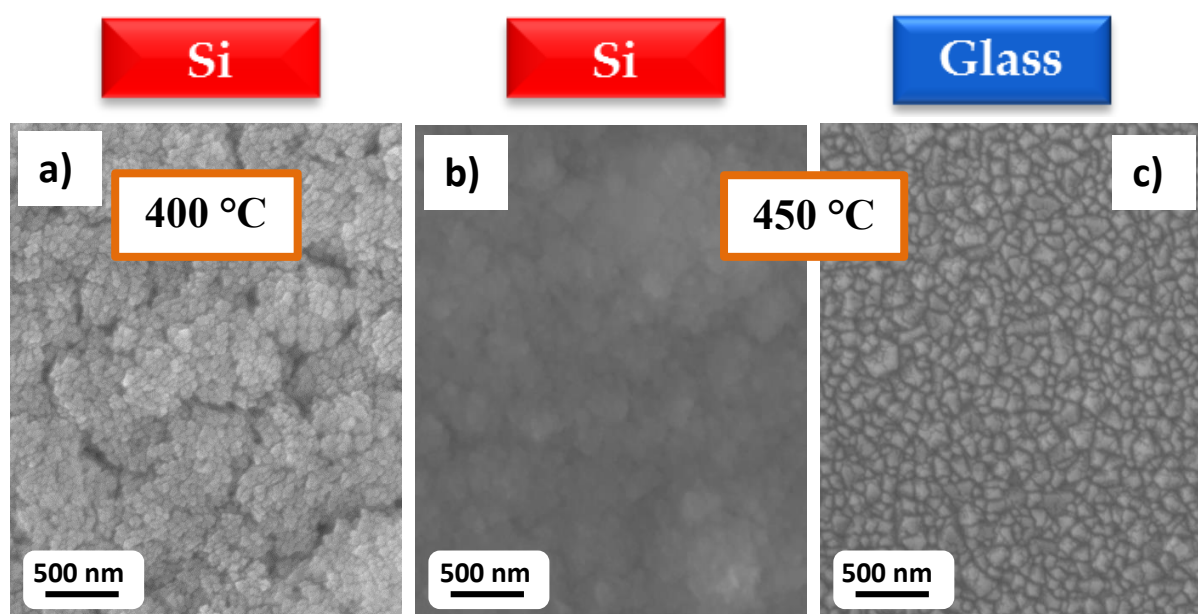


Fig. 8 FE-SEM images of MOCVD  $\text{CaF}_2: \text{Yb}(18\%), \text{Er}(2\%), \text{Tm}(1\%)$  films deposited at 400 °C on Si (a), 450 °C on Si (b), and 450 °C on glass (c).

These films have diffraction patterns similar to the one of the  $\text{CaF}_2: \text{Yb}^{3+}, \text{Er}^{3+}$  film deposited at 500 °C on Si.<sup>24</sup> A typical pattern of the  $\text{CaF}_2: \text{Yb}^{3+}(18\%), \text{Er}^{3+}(2\%), \text{Tm}^{3+}(1\%)$  film deposited at 400 °C is reported in Fig. S7 (ESI<sup>†</sup>).

#### Upconversion properties for thin films prepared by sol-gel.

Upconversion spectra for the  $\text{CaF}_2: \text{Yb}^{3+}(18\%): \text{Er}^{3+}(2\%): \text{Tm}^{3+}(1\%)$  thin films prepared by sol-gel and annealed at 350 and 400 °C on glass substrate are shown in Fig. 9 and Fig. S8 (ESI<sup>†</sup>), respectively. Typical emission bands due to  $\text{Er}^{3+}$  ions and  $\text{Tm}^{3+}$  ions in the visible and near infrared region (NIR) are shown, indicating that these ions are present, although too diluted to be detected with the EDX technique, as described above. The assignments of the emission band to the lanthanide transitions are indicated in the caption of Fig. 9 and S8 (ESI) and the upconversion mechanisms following 980 nm excitation are shown in Fig. 10. The emission profile for each band is very similar for samples prepared at different temperatures, indicating that the local crystal fields experienced by the lanthanide ions are similar. The relative intensities of the emission bands with respect to the strongest one in the red region (around 650 nm) are similar for the samples prepared at 350 and 400 °C. One evident difference of the UC spectra is the relative intensity of the  $\text{Tm}^{3+}$  emission band around 470 nm, that is slightly

stronger for the sample annealed at 350 °C (see Fig. 9 and Fig.

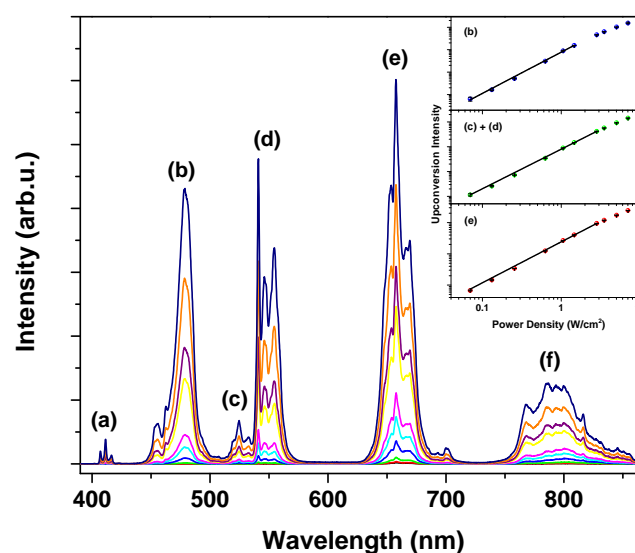
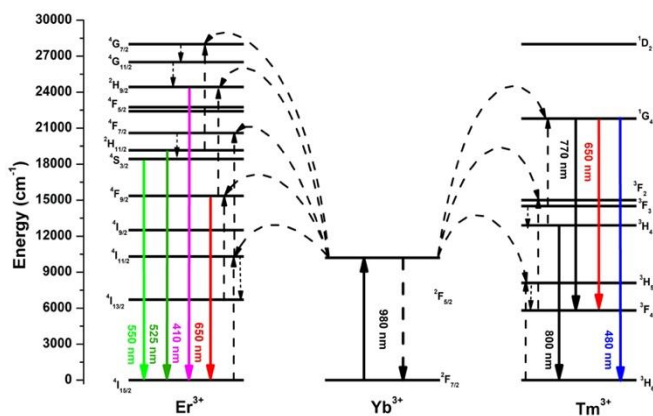


Fig. 9. Upconversion spectra as a function of the laser power for the  $\text{CaF}_2: \text{Yb}^{3+}(18\%): \text{Er}^{3+}(2\%): \text{Tm}^{3+}(1\%)$  thin film on glass deposited by the sol-gel technique and annealed at 350 °C. Bands attribution: (a)  $\text{Er}^{3+}, {}^2\text{H}_{9/2} \rightarrow {}^4\text{I}_{15/2}$ ; (b)  $\text{Tm}^{3+}, {}^1\text{G}_4 \rightarrow {}^3\text{H}_6$ ; (c)  $\text{Er}^{3+}, {}^2\text{H}_{11/2} \rightarrow {}^4\text{I}_{15/2}$ ; (d)  $\text{Er}^{3+}, {}^4\text{S}_{3/2} \rightarrow {}^4\text{I}_{15/2}$ ; (e)  $\text{Er}^{3+}, {}^4\text{F}_{9/2} \rightarrow {}^4\text{I}_{15/2}$ ;  $\text{Tm}^{3+}, {}^1\text{G}_4 \rightarrow {}^3\text{F}_4$ ; (f)  $\text{Tm}^{3+}, {}^3\text{H}_4 \rightarrow {}^3\text{H}_6$ . Inset: upconversion power study.





**Figure 10.** Energy level scheme for the Yb<sup>3+</sup>, Er<sup>3+</sup> and Tm<sup>3+</sup> ions. Solid arrows: radiative transitions. Dashed arrows: energy transfer processes. Dotted arrows: non-radiative transitions.

S8, ESI<sup>†</sup>). This behaviour could be due to different efficiencies of the energy transfer processes among the Er<sup>3+</sup> and Tm<sup>3+</sup> ions, due to slightly different lanthanide ions average distances. It can be also correlated to the different crystallinity as well as to the domain size of the samples annealed at different temperatures, as indicated by the X-Ray diffraction patterns, see Fig. 1. In particular, the heat treatment at 400 °C generates a more crystalline sample than that annealed at 350 °C. The difference in the relative intensities for the Er<sup>3+</sup> and Tm<sup>3+</sup> emissions is particularly evident for heavy doped Tm<sup>3+</sup> and Er<sup>3+</sup> CaF<sub>2</sub> thin film samples, as described below for the samples prepared through the MOCVD technique. In order to evaluate the upconversion emission efficiency of the obtained thin films, we adopted an alternative method with respect to the much more difficult measurement of the upconversion quantum efficiency using an integrating sphere. Our simpler method is based on the measurements of the minimum power density of the exciting laser source needed to generate emissions that can be detected by the present experimental setup, very similar to those commonly used in typical spectroscopy laboratories (see experimental section). Therefore, the upconversion spectra of some emission bands for Er<sup>3+</sup> and Tm<sup>3+</sup> ions were measured as a function of the laser power and they are shown in the insets of Fig. 9 and Fig. S8 (ESI<sup>†</sup>) for the samples prepared by sol-gel technique and annealed at 350 and 400 °C, respectively. As typical for upconversion emissions, at low laser power densities, we found a behaviour in agreement with the equation:<sup>26</sup>

$$I(UC) \propto P^n$$

where  $I(UC)$  represents the upconversion intensity,  $P$  is the laser power and  $n$  is the order of the upconversion process. The slopes of the fits of the power studies for the sol-gel samples, typically  $n > 1$ , are shown in Table S2 (ESI<sup>†</sup>), and found in agreement with those reported for a Er<sup>3+</sup>, Tm<sup>3+</sup>, Yb<sup>3+</sup> tridoped CaF<sub>2</sub> single crystal.<sup>27</sup> Most interestingly, the lowest laser powers at which upconversion signals were observed around 70 mW/cm<sup>2</sup> and 90 mW/cm<sup>2</sup> for the samples annealed at 350 °C and 400 °C, respectively. It is worth to underline that no papers on alkaline-earth CaF<sub>2</sub> or SrF<sub>2</sub> upconverting thin films reports any information about the upconversion

efficiency of the materials. On the other hand, few papers have been published describing the upconversion properties of Er<sup>3+</sup> and Yb<sup>3+</sup> doped NaYF<sub>4</sub> thin films,<sup>19,28</sup> but quantitative data on the upconversion efficiency of such thin films are still missing. Although some power studies on Er<sup>3+</sup>-Yb<sup>3+</sup> codoped upconverting fluoride-based nanoparticles have been reported in the literature,<sup>[29]</sup> it is not easy to directly compare those results with our experimental data. In fact, while in our samples the laser optical path inside the sample on which the experiments have been carried out is well known (film thickness of 700-750 nm, see Fig. 3 above), no optical paths for the laser excitation radiation are reported for the investigated samples in literature.<sup>[29]</sup> We expect, in fact, that the upconversion emissions strongly depend on the active volume of sample involved in the generation of the upconversion emission. Nonetheless, in a quite recent paper, Fan et al.<sup>30</sup> reported that microparticles of Er<sup>3+</sup>, Yb<sup>3+</sup> doped  $\beta$ -NaYF<sub>4</sub>, a material which is among the most efficient upconverters, show a minimum power density for the upconversion power study of 700 mW/cm<sup>2</sup> while a minimum value of 400 mW/cm<sup>2</sup> was used for evaluation of the absolute emission quantum yield. In our systems, the minimum values of the laser power needed in the present samples (70 mW/cm<sup>2</sup> and 90 mW/cm<sup>2</sup>, for the 350 °C and 400 °C samples, respectively) points to a very high upconversion efficiency.

In order to gain information on the excited state dynamics of the lanthanide ions in the thin films, we measured the decay curves of the upconversion emissions, shown in Fig. 11. As can be noted, the decay curves show a non-exponential decay for emission originating from both Tm<sup>3+</sup> and Er<sup>3+</sup> ions. This behaviour is most probably due to slightly distorted environment in which the lanthanide ions are accommodated as well as to energy transfer processes among the lanthanide ions. Due to the non-exponential nature, the lifetimes of the lanthanide ion energy levels have been estimated by the time elapsed to decrease the emission intensity from the initial value  $I_0$  (for  $t=0$ ) to  $I_0/e$ .

The obtained lifetimes for the Tm<sup>3+</sup> and Er<sup>3+</sup> ions and

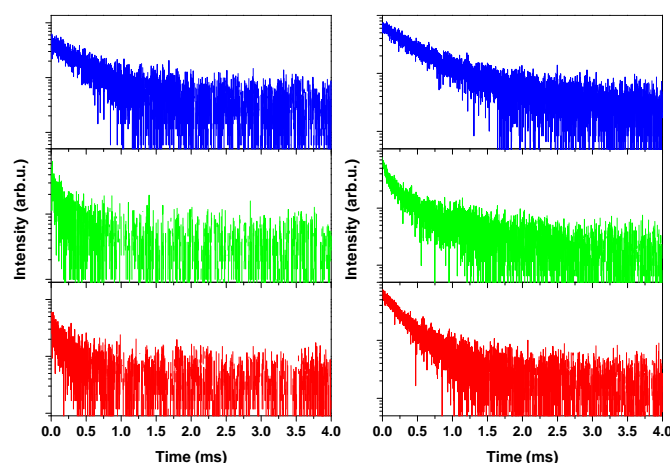
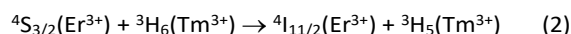
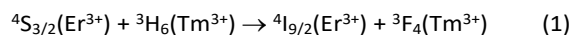


**Fig. 11** Emission decay curves for the CaF<sub>2</sub>:Yb<sup>3+</sup>(18%):Er<sup>3+</sup>(2%):Tm<sup>3+</sup>(1%) thin film on glass substrate deposited by sol-gel technique and annealed at 350 °C (left) and 400 °C (right). Blue line:  $\lambda_{em}=480$  nm; green line:  $\lambda_{em}=550$  nm; red line:  $\lambda_{em}=660$  nm.



uncertainties for the two samples prepared by sol-gel at 350 °C and 400 °C are reported in Table 2. The experimental decay times for the  $^4S_{3/2}$  level of the  $Er^{3+}$  ion in both samples ( $120 \pm 43 \mu s$  and  $184 \pm 9 \mu s$ ) appear to be lower than the radiative lifetime ( $565 \mu s$ ) calculated for an  $Er^{3+}$  doped  $CaF_2$  single crystal.<sup>31</sup> This behavior indicates that non-radiative processes are present in the thin films, as multiphonon relaxations as well as possible energy transfers from the  $Er^{3+}$  to other lanthanide ions, as  $Tm^{3+}$  ones. Also, the decay time for the  $^1G_4$  level of  $Tm^{3+}$  ions is significantly lower than that observed for a  $Tm^{3+}$  doped  $CaF_2$  single crystal<sup>32</sup> (1.1 ms for a center with  $C_{3v}$  site symmetry), suggesting again the presence of non-radiative relaxations in the present samples. Moreover, the lifetimes for both  $Er^{3+}$  and  $Tm^{3+}$  ions appear to be significantly longer for the sample annealed at 400 °C than for the one annealed at 350 °C. This behaviour could be explained by a slightly less distorted average local environment around the lanthanide ions due to the higher crystallinity of the sample as well as to larger domain size caused by annealing at higher temperature. This is in agreement with the results obtained by the X-ray diffraction patterns and also by the upconversion spectra. Due to non-negligible concentrations of the  $Er^{3+}$  (2%) and  $Tm^{3+}$  (1%) ions in the crystalline host, it is conceivable that energy transfer (ET) processes between lanthanide ions (i.e. between  $Tm^{3+}$  and  $Er^{3+}$ ) are present, in particular involving the  $^4S_{3/2}$  and the  $^4F_{9/2}$  excited energy levels of the  $Er^{3+}$  ions. In fact, Yeh et al.<sup>33</sup> found, for a  $Er^{3+}$  and  $Tm^{3+}$  codoped barium-thorium fluoride glass, several  $Er^{3+} \rightarrow Tm^{3+}$  energy transfer processes, in particular involving the  $^4S_{3/2}$  energy level of the  $Er^{3+}$  ion, described by the ET mechanisms:<sup>33</sup>



Other energy transfer processes can involve the  $^4F_{9/2}$  energy level of the  $Er^{3+}$  ion:

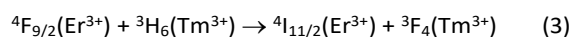
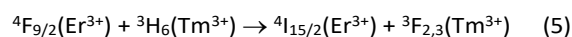
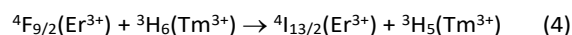
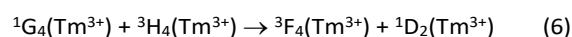


**Table 2.** Decay times for the  $CaF_2:Yb^{3+}(18\%):Er^{3+}(2\%):Tm^{3+}(1\%)$  thin films prepared by sol-gel technique on glass substrate obtained from the emission decay curves shown in Fig. 11. The decay times refer to the two annealing temperatures in the sol-gel procedure.

Transition	350 °C	400 °C
$^1G_4 \rightarrow ^3H_6 (Tm^{3+})$ $\lambda_{em}=480 \text{ nm}$	(504 ± 37) $\mu s$	(541 ± 9) $\mu s$
$^4S_{3/2} \rightarrow ^4I_{15/2} (Er^{3+})$ $\lambda_{em}=550 \text{ nm}$	(120 ± 43) $\mu s$	(184 ± 9) $\mu s$
$^4F_{9/2} \rightarrow ^4I_{15/2} (Er^{3+})$ $^1G_4 \rightarrow ^3F_4 (Tm^{3+})$ $\lambda_{em}=660 \text{ nm}$	(230 ± 46) $\mu s$	(303 ± 9) $\mu s$



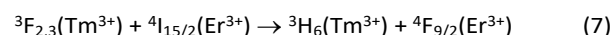
These possible  $Er^{3+} \rightarrow Tm^{3+}$  energy transfer processes for our upconverting systems are shown in Fig. S9a (ESI<sup>†</sup>). Relevant  $Er^{3+}$ - $Tm^{3+}$  energy transfers, in line with the results obtained in the present investigation, were also found by Rivera et al. for  $Er^{3+}$ - $Tm^{3+}$  codoped germanium-tellurite glasses.<sup>34</sup> Furthermore, the non-exponential nature of the emission decay curve for the  $Tm^{3+}$  ion can also be due to cross-relaxations between  $Tm^{3+}$  ions, as underlined by Wang et al for  $NaYF_4:Yb^{3+}, Tm^{3+}$  microcrystals,<sup>35</sup> described by the ET mechanism (see Fig. S9b, ESI<sup>†</sup>):



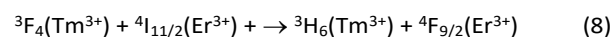
This mechanism can induce the shortening of the  $^1G_4$  energy level lifetime of the  $Tm^{3+}$  ions with respect to that observed for a  $Tm^{3+}$  doped  $CaF_2$  single crystal,<sup>32</sup> as in fact observed for the present thin film samples (see Table 2).

#### Upconversion properties of thin films prepared by MOCVD.

Tridoped  $Er^{3+}$ ,  $Tm^{3+}$  and  $Yb^{3+}$  heavy doped samples (10%  $Er^{3+}$ , 10%  $Tm^{3+}$  and 10%  $Yb^{3+}$  ions concentration) were prepared by MOCVD technique at two different reaction temperatures, at 400 and 450 °C. Their upconversion spectra are shown in Fig. S10 (ESI<sup>†</sup>). Emissions in the 500-550 nm green region and in the 625-700 nm region are observed and easily assigned to the  $Er^{3+}$  ions. It has to be noted that only a very weak emission band observed around 800 nm can be attributed to  $Tm^{3+}$  ions. This behaviour is due to very efficient  $Tm^{3+} \rightarrow Er^{3+}$  energy transfer processes, suggested by Rivera et al.:<sup>34</sup>



and also by Chan et al.<sup>36</sup>



that are very relevant for high doping levels for both  $Tm^{3+}$  and  $Er^{3+}$  ions (see Fig. S9c, ESI<sup>†</sup>). It is worth to note that both (7) and (8) mechanisms can induce an increased population of the  $^4F_{9/2}$  level of the  $Er^{3+}$  ions and therefore, in turn, an increase of intensity of the band at 660 nm due to the  $^4F_{9/2} \rightarrow ^4I_{15/2}$  transition. In fact, from Fig. S10 (ESI<sup>†</sup>) it can be noted that the relative intensity of the band at 660 nm is much higher with respect to those observed in the 500-550 nm green region, corroborating the presence of the abovementioned mechanisms increasing the population of the  $^4F_{9/2}$  level of the  $Er^{3+}$  ions.

The upconversion spectra for the tri-doped  $CaF_2:Yb^{3+}(18\%):Er^{3+}(2\%):Tm^{3+}(1\%)$  thin films deposited on glass through MOCVD at 450 °C and 400 °C are shown in Fig. 12 and Fig. S11 (ESI<sup>†</sup>), respectively.

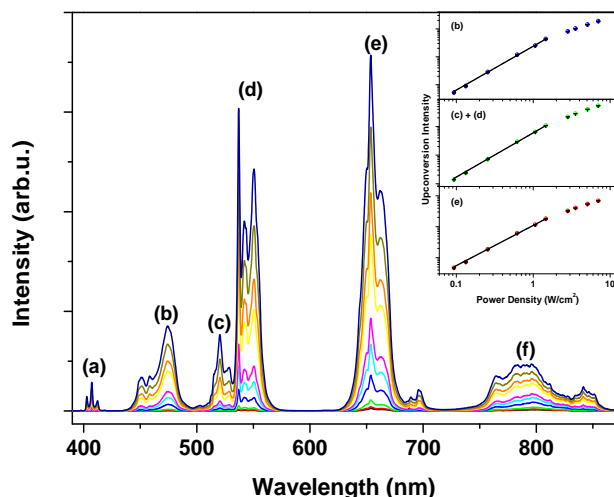


Fig. 12 Upconversion spectra as a function of the laser power density for the  $\text{CaF}_2:\text{Yb}_3+(18\%):\text{Er}_3+(2\%):\text{Tm}_3+(1\%)$  film deposited on quartz by MOCVD at 450 °C. Bands attribution: (a)  $\text{Er}^{3+}$ ,  $2\text{H}_9/2 \rightarrow 4\text{I}_{15}/2$ ; (b)  $\text{Tm}^{3+}$ ,  $1\text{G}_4 \rightarrow 3\text{H}_6$ ; (c)  $\text{Er}^{3+}$ ,  $2\text{H}_{11}/2 \rightarrow 4\text{I}_{15}/2$ ; (d)  $\text{Er}^{3+}$ ,  $4\text{S}_3/2 \rightarrow 4\text{I}_{15}/2$ ; (e)  $\text{Er}^{3+}$ ,  $4\text{F}_9/2 \rightarrow 4\text{I}_{15}/2$ ;  $\text{Tm}^{3+}$ ,  $1\text{G}_4 \rightarrow 3\text{F}_4$ ; (f)  $\text{Tm}^{3+}$ ,  $3\text{H}_4 \rightarrow 3\text{H}_6$ . Inset: upconversion power study.

Emission bands due to  $\text{Er}^{3+}$  ions and  $\text{Tm}^{3+}$  ions in the visible and near infrared region (NIR) are evident, and the spectra are similar to those observed for the samples prepared by the sol-gel technique. In this case, the emission spectra for samples prepared at different deposition temperatures appear to be very similar, indicating that the local crystalline environment around the lanthanide ions is barely influenced by the difference in deposition temperature. This observation may be explained considering that at 400 °C the film have already a good crystalline structure (Fig. 6). In analogy with the samples prepared using the sol-gel technique, the upconversion spectra of the emission bands were measured as a function of the laser power. The integrated emissions vs. laser power density are shown in the insets of Fig. 12 and Fig. S11 (ESI<sup>†</sup>), for deposition temperatures of 450 and 400 °C, respectively. From the fit of these curves with a straight line we obtained their slopes that are shown in Table S3 (ESI<sup>†</sup>).

Table 3. Decay times for the  $\text{CaF}_2:\text{Yb}_3+(18\%):\text{Er}_3+(2\%):\text{Tm}_3+(1\%)$  thin films prepared by MOCVD technique on glass substrate, obtained from the emission decay curves shown in Fig. 12. The decay times refer to the two reaction temperatures in the MOCVD procedure.

Transition	400 °C	450 °C
$^1\text{G}_4 \rightarrow ^3\text{H}_6$ ( $\text{Tm}^{3+}$ ) $\lambda_{\text{em}}=480$ nm	$(180 \pm 35)$ $\mu\text{s}$	$(245 \pm 55)$ $\mu\text{s}$
$^4\text{S}_{3/2} \rightarrow ^4\text{I}_{15/2}$ ( $\text{Er}^{3+}$ ) $\lambda_{\text{em}}=550$ nm	$(77 \pm 20)$ $\mu\text{s}$	$(86 \pm 10)$ $\mu\text{s}$
$^4\text{F}_{9/2} \rightarrow ^4\text{I}_{15/2}$ ( $\text{Er}^{3+}$ ) $^1\text{G}_4 \rightarrow ^3\text{F}_4$ ( $\text{Tm}^{3+}$ ) $\lambda_{\text{em}}=660$ nm	$(150 \pm 43)$ $\mu\text{s}$	$(197 \pm 38)$ $\mu\text{s}$

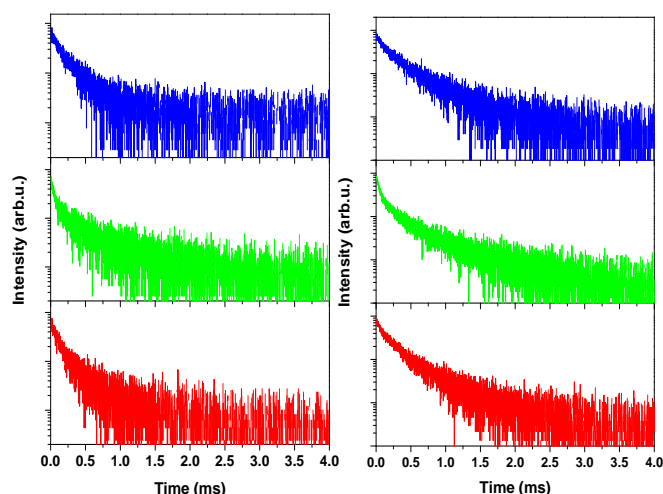


Fig. 13 Emission decays for the tri-doped  $\text{CaF}_2:\text{Yb}_3+(18\%):\text{Er}_3+(2\%):\text{Tm}_3+(1\%)$  thin film deposited on quartz through MOCVD at 400 °C (left) and 450 °C (right). Blue line:  $\lambda_{\text{em}}=480$  nm; green line:  $\lambda_{\text{em}}=550$  nm; red line:  $\lambda_{\text{em}}=660$  nm.

It is worth noting that also in these cases we were able to measure significant emissions, both in the green and red regions, at a laser power density as low as 100  $\text{mW}/\text{cm}^2$  for both the samples (see Fig. 12 and Fig. S10 (ESI), similarly to what found for the sol-gel prepared samples (see Fig. 9), suggesting an efficient upconversion emission upon 980 nm laser excitation.

The decay curves for the emission of  $\text{Tm}^{3+}$  and  $\text{Er}^{3+}$  ions embedded in the crystal host for the MOCVD prepared thin films are shown in Fig. 13. In all cases a non-exponential behaviour of the curves are noted, and lifetimes for the MOCVD grown films, obtained using the same procedure

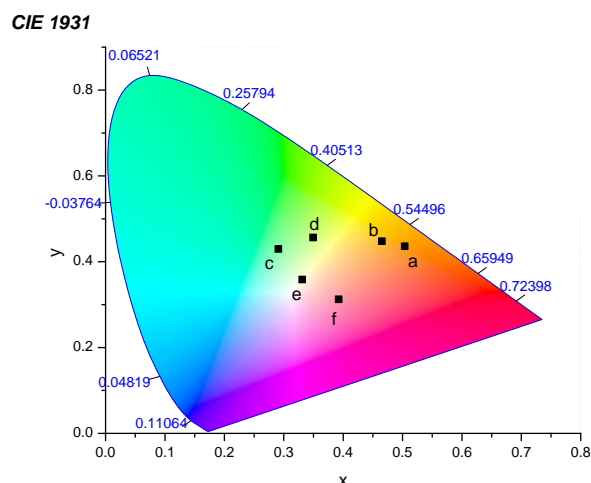


Fig. 14 CIE 1931 color coordinates: (a)  $\text{CaF}_2:\text{Yb}10\%,\text{Tm}10\%,\text{Er}10\%$  (MOCVD, 400 °C); (b)  $\text{CaF}_2:\text{Yb}10\%,\text{Tm}10\%,\text{Er}10\%$  (MOCVD, 450 °C); (c)  $\text{CaF}_2:\text{Yb}18\%,\text{Tm}1\%,\text{Er}2\%$  (MOCVD, 400 °C); (d)  $\text{CaF}_2:\text{Yb}18\%,\text{Tm}1\%,\text{Er}2\%$  (MOCVD, 450 °C); (e)  $\text{CaF}_2:\text{Yb}18\%,\text{Tm}1\%,\text{Er}2\%$  (sol-gel, 350 °C); (f)  $\text{CaF}_2:\text{Yb}18\%,\text{Tm}1\%,\text{Er}2\%$  (sol-gel, 400 °C).

described above for the sol-gel prepared samples, are reported in Table 3. The lifetimes are slightly shorter than those obtained for the sol-gel prepared samples (cf. With Table 2).

This behaviour suggests a slightly more distorted environment for the lanthanide ions in the crystal lattice that induces a shortening of the lifetimes with respect to the sol-gel prepared samples.

In order to investigate the colour properties of the emission of the tri-doped samples, a chromaticity coordinate analysis was carried out on all the UC spectra. This analysis is an important tool to understand how the human eye will perceive the color of a certain emission. It consists in weighing an emission spectrum with the response of the cones of the retina of a human eye to radiation in the Red, Green and Blue (RGB) ranges. The color coordinates are plotted in the CIE 1931 space. The color coordinates were calculated for the emission spectra obtained at the maximum excitation power and they are shown in Fig. 14. As it can be easily noted from Fig. 14, emissions of the heavily lanthanide doped samples (prepared by MOCVD, shows as (a) and (b) coordinates) lies in the orange region of the CIE 1931 color space.

This is due to the lack of blue emission from  $\text{Tm}^{3+}$  ions. On the other hand, the MOCVD and sol-gel samples doped with 18%  $\text{Yb}^{3+}$ , 2% $\text{Er}^{3+}$  and 1% $\text{Tm}^{3+}$  show color coordinates located in the central part of the CIE 1931 color space, due to the presence of the blue emission of  $\text{Tm}^{3+}$  ions ((c), (d), (e) and (f) points in Fig. 14). In particular, the sol-gel sample heat treated at 350 °C shows an almost perfectly white emission with (0.33, 0.36) color coordinates.

## Conclusions

A comparison between vapor phase and solution route approaches for the preparation of pure and Ln doped  $\text{CaF}_2$  thin films has been reported using the same starting reagents, i.e.  $\beta$ -diketonate glyme adducts. Both methods are reliable and reproducible, and moreover the fluorinated metal precursors act efficiently as single-sources, thus avoiding the use of external fluorine sources during the synthetic processes. The morphologies of the doped films are quite uniform, with the MOCVD grown layers having a better homogeneity. Thus, the present results indicate that both methods are appealing strategies for preparing these materials on different substrates. A balance of pros and cons between the two synthetic approaches designates the present MOCVD method as a fast, compared to the aging time needed in sol-gel, and industrially appealing process, due to its easy scalability. On the other hand, sol-gel, if combined with a spraying deposition procedure, would have the advantage of being a low cost approach with a great potential for scaling up. The  $\text{Yb}^{3+}$ ,  $\text{Er}^{3+}$ ,  $\text{Tm}^{3+}$  ions tri-doped  $\text{CaF}_2$  thin films show a strong upconversion emission, especially in the visible region, with features typical of these lanthanide ions. In fact, the power studies indicate that the upconversion emission can be generated with relatively low laser power densities, pointing to very good upconversion efficiencies for both the sol-gel/spin-coated and

MOCVD prepared  $\text{Yb}^{3+}$ ,  $\text{Er}^{3+}$ ,  $\text{Tm}^{3+}$  ions tri-doped  $\text{CaF}_2$  thin films. Color coordinates indicate that the UC emission is in the central region of the CIE1931 color space. For one sample, an almost perfectly white emission with (0.33, 0.36) color coordinates was obtained, thus these systems have the potential to be used as efficient emitting systems in optic applications.

## Conflicts of interest

There are no conflicts to declare.

## Acknowledgements

The authors thank the University of Catania for financial support within the "CHANCE" project and the University of Verona for funding in the framework of the project "Joint Projects 2018". A. L. P. and G. M. thank Bio-nanotech Research and Innovation Tower (BRIT) laboratory of University of Catania for the diffractometer facility.

## References

- 1 a) A. Tressaud, K. Poeppelmeier, *Photonic and electronic properties of fluoride materials*, Elsevier, Amsterdam, Netherlands, 2016; b) K. Scheurell, E. Kemnitz, *Inorganics*, 2018, **6**, 128/1-128/19 ; c) M. P. Remington, Jr, Eur. Pat. Appl. 2009, 18pp; d) T. Pilvi, M. Ritala, M. Leskela, M. Bischoff, U. Kaiser, N. Kaiser, *Appl. Opt.* 2008, **47**, C271-C274; e) F. Perales, J. M. Herrero, D. Jaque, C. de las Heras, *Opt. Mater.* 2007, **29**, 783-787; f) S. Fujihara, K. Tokumo, *J. Fluorine Chem.* 2009, **130**, 1106-1110.
- 2 a) M. Quintanilla, I. X. Cantarelli, M. Pedroni, A. Speghini and F. Vetrone, *J. Mater. Chem. C* 2015, **3**, 3108-3113; b) M. Back, R. Marin, M. Franceschin, N. Sfar Hancha, F. Enrichi, E. Trave and S. Polizzi, *J. Mater. Chem. C* 2016, **4**, 1906-1913; c) V. Mahalingam, K. N. K. B. Adusumalli and M. Koppsetti, *J. Mater. Chem. C* 2016, **4**, 2289-2294; d) B. Ritter, P. Haida, F. Fink, T. Krahl, K. Gawlitza, K. Rurack, E. Kemnitz, *Dalton Trans.* 2017, **46**, 2925-2936; e) T. Gu, L. Cheng, F. Gong, J. Xu, X. Li, G. Han and Z. Liu, *ACS Appl. Mater. Interfaces*, 2018, **10**, 15494-15503; f) F. Vetrone, R. Naccache, V. Mahalingam, C. G. Morgan and J. A. Capobianco, *Adv. Funct. Mater.*, 2009, **19**, 2924-2929.
- 3 a) B. McKenna and R. C. Evans, *Adv. Mater.*, 2017, **29**, 1606491/1-23; b) I. Etxebarria, J. Ajuria and R. Pacios, *Organic Electronics*, 2015, **19**, 34-60.
- 4 a) Q. Sun, G. Hu, Z. Lin, L. Yu, X. Liu and Y. Yu, *Adv. Mater. Res.*, 2014, **827**, 44-48; b) M. He, X. Pang, X. Liu, B. Jiang, H. He, H. Snaith and Z. Lin, *Angew. Chemie*, 2016, **55**, 4280-4284.
- 5 a) F. Kaholi, N. Ghazyani, M. Riahi, H. Zare-Behtash, M. H. M. Ara and E. Heydari, *Acs Appl. Nano Mater.*, 2019, **2**, 3590-3596; b) F. Gonell, A. M. P. Botas, C. D. S. Brites, P. Amoros, L. D. Carlos, B. Julian-Lopez and R. A. S. Ferreira, *Nanoscale Adv.*, 2019, **1**, 2537-2545.
- 6 a) D. Q. Chen, M. Xu and P. Huang, *Sensor Actuat. B-Chem.*, 2016, **231**, 576-583; b) M. Y. Ding, D. Q. Chen, D. Y. Ma, J. B. Dai, Y. T. Li and Z. G. Ji, *J. Mater. Chem. C*, 2016, **4**, 2432-2437; c) G. Tessitore, S. L. Maurizio, T. Sabri and J. A. Capobianco, *Angew. Chem. Int. Edit.*, 2019, **58**, 9742-9751.

- 7 a) T. Cheng, R. Marin, A. Skripka and F. Vetrone, *J Am Chem Soc*, 2018, **140**, 12890-12899; b) D. Sarkar, S. Ganguli, T. Samanta and V. Mahalingam, *Langmuir*, 2019, **35**, 6211-6230.
- 8 F. Auzel, *J. Lumin.*, 1990, **45**, 341-345.
- 9 C. Cao, W. Qin, J. Zhang, Y. Wang, G. Wang, G. Wei, P. Zhu, L. Wang and L. Jin, *Optics Communications*, 2008, **281**, 1716-1719.
- 10 Y. Hao, S. Lv, Z. Ma and J. Qiu, *RSC Advances*, 2018, **8**, 12165-12172.
- 11 S. Normani, A. Braud, R. Soulard, J. L. Doualan, A. Benayad, V. Menard, G. Brasse, R. Moncorge, J. P. Goossens and P. Camy, *CrystEngComm*, 2016, **18**, 9016-9025.
- 12 a) L. Pinol, K. Rebello, K. Caruso, A. S. Francomacaro and G. L. Coles, *J. Vacuum Sci. Technol.*, 2011, **29**, 021001/1-4; b) H.-F. Li, T. Parker, F. Tang, G.-C. Wang, T.-M. Lu and S. Lee, *J. Crystal Growth*, 2008, **310**, 3610-3614.
- 13 R. K. Pandey, M. Kumar, S. A. Khan, T. Kumar, A. Tripathi, D. K. Avasthi and A. C. Pandey, *Appl. Surf. Sci.* 2014, **289**, 77-80.
- 14 C. Deiter, M. Bierkandt, A. Klust, C. Kumpf, Y. Su, O. Bunk, R. Feidenhans'l and J. Wollschläger, *Phys. Rev. B* 2010, **82**, 085449/1-11.
- 15 T. Jiang, W. Qin and F. Ding, *J. Nanosci. Nanotechnol.*, 2010, **10**, 2013-2016.
- 16 a) M. Ylilammi and T. Ranta-aho, *J. Electrochem. Soc.*, 1994, **141**, 1278-1284; b) T. Pilvi, K. Arstila, M. Leskela and M. Ritala, *Chem. Mater.*, 2007, **19**, 3387-3392; c) A. M. Makarevich, A. S. Shchukin, A. V. Markelov, S. V. Samoilenkov, P. P. Semyannikov, N. P. Kuzmina, *ECS Transactions*, 2009, **25**, 525-532.
- 17 a) Q. Zeng, B. Xue, Y. Zhang, D. Wang, X. Liu, L. Tu, H. Zhao, X. Kong and H. Zhang, *Cryst Eng Comm*, 2013, **15**, 4765-4772; b) D. Thangaraju, V. Santhana, S. Matsuda and Y. Hayakawa, *J. Electronic Mater.*, 2018, **47**, 4555-4560; c) R. Wang, X. Li, L. Zhou and F. Zhang, *Angewandte Chemie Int. Ed.*, 2014, **53**, 12086-12090.
- 18 a) H. Jia, C. Xu, J. Wang, P. Chen, X. Liu and J. Qiu, *Cryst Eng Comm*, 2014, **16**, 4023-4028; b) Z. Jia, K. Zheng, D. Zhang, D. Zhao and W. Qin, *J. Nanosci. Nanotechnol.*, 2011, **11**, 9690-9692; c) H. Park, G. Y. Yoo, M. S. Kim, K. Kim, C. Lee, S. Park, S. and W. Kim, *J. Alloys Comp.*, 2017, **728**, 927-935.
- 19 a) A. L. Pellegrino, M. R. Catalano, P. Cortelletti, G. Lucchini, A. Speghini and G. Malandrino, *Photochem. Photobio. Sci.*, 2018, **17**, 1239-1246; b) M. R. Catalano, A. L. Pellegrino, P. Rossi, P. Paoli, P. Cortelletti, M. Pedroni, A. Speghini, and G. Malandrino, *New J. Chem.*, 2017, **41**, 4771-4775.
- 20 a) N. P. Kuzmina, D. M. Tsybarenko, I. E. Korsakov, Z. A. Starikova, K. A. Lysenko, Olga V. Boytsova, A. V. Mironov, I. P. Malkerova and A. S. Alikhanyan, *Polyhedron*, 2008, **27**, 2811-2818; b) A. M. Makarevich, P. P. Semyannikov and N. P. Kuzmina, *Russ. J. Inorg. Chem.*, 2010, **55**, 1940-1943; c) D. M. Tsybarenko, A. V. Mironov, S. N. Mudretsova, A. M. Makarevich and N. P. Kuzmina, *Polyhedron*, 2011, **30**, 599-605
- 21 a) A. Valore, E. Cariati, S. Righetto, D. Roberto, F. Tessore, R. Ugo, I. L. Fragalà, M. E. Fragalà, G. Malandrino, F. De Angelis, L. Belpassi, I. Ledoux-Rak, K. H. Thi and J. Zyss, *J. Am. Chem. Soc.*, 2010, **132**, 4966-4970; b) G. Malandrino and I. L. Fragalà, *Coord. Chem. Rev.*, 2006, **250**, 1605-1620.
- 22 C.-K. Chiu, T.-Y. Chen, M. T.-J. Luo, *Adv. Eng. Mater.*, 2013, **15**, 34-39.
- 23 S. Fujihara, Y. Kadota, and T. Kimura, *J. Sol-Gel Sci. Technol.*, 2002, **24**, 147-154.
- 24 A. L. Pellegrino, P. Cortelletti, M. Pedroni, A. Speghini and G. Malandrino, *Adv. Mater. Interfaces*, 2017, **4**, 1700245/1-6.
- 25 I. X. Cantarelli, M. Pedroni, F. Piccinelli, P. Marzola, F. Boschi, G. Conti, A. Sbarbati, P. Bernardi, E. Mosconi, L. Perbellini, L. Marongiu, M. Donini, S. Dusi, L. Sorace, C. Innocenti, E. Fantechi, C. Sangregorio and A. Speghini, *Biomater. Sci.*, 2014, **2**, 1158-1171.
- 26 M. Pollnau, D. R. Gamelin, S. R. Luthi, H. U. Gudel and M. P. Hehlen, *Phys. Rev. B*, 2000, **61**, 3337-3346.
- 27 X. Y. Chen, B. Zhang, X. B. Qian, J. Y. Wang, L. L. Zheng, J. S. Hou, Y. Z. Fang and L. B. Su, *Opt. Mater.*, 2019, **90**, 40-45.
- 28 a) Q. R. Zhao, J. Zhao, M. Tao, C. Wang, X. Q. Zeng, Y. M. Hu, S. F. Wang, M. H. Zeng, W. Zhou, H. S. Gu and Y. B. Li, *J. Lumin.*, 2019, **214**, 116580; b) L. J. Zhang, L. L. Tian, H. Wang, X. Zhang, J. Y. Gong and R. Liu, *Ecs. J Solid State Sc.*, 2018, **7**, R120-R124; c) H. Park, G. Y. Yoo, M. S. Kim, K. Kim, C. Lee, S. Park and W. Kim, *J. Alloy Compd.*, 2017, **728**, 927-935.
- 29 a) A. Kar, S. Kundu and A. Patra, *ChemPhysChem*, 2015, **16**, 505-521; b) O. A. Savchuk, J. J. Carvajal, Y. Cesteros, P. Salagre, H. D. Nguyen, A. Rodenas, J. Massons, M. Aguilo, Magdalena and F. Diaz, *Front. Chem.*, 2019, **7**, 88; c) S. Fischer, R. D. Mehlenbacher, A. Lay, C. Siefe, A. P. Alivisatos, and J. A. Dionne, *Nano Lett.*, 2019, **19**, 3878-3885.
- 30 S. H. Fan, G. J. Gao, S. Y. Sun, S. J. Fan, H. T. Sun and L. L. Hu, *J. Mater. Chem. C*, 2018, **6**, 5453-5461.
- 31 E. Preda, M. Stef, G. Buse, A. Pruna and I. Nicoara, *Phys. Scripta*, 2009, **79**.
- 32 N. M. Strickland and G. D. Jones, *Phys. Rev. B*, 1997, **56**, 10916-10929.
- 33 D. C. Yeh, R. R. Petrin, W. A. Sibley, V. Madigou, J. L. Adam and M. J. Suscavage, *Phys. Rev. B*, 1989, **39**, 80-90.
- 34 V. A. G. Rivera, Y. Ledemi, M. El-Amraoui, Y. Messaddeq and E. Marega, *J Non-Crys.t Solids*, 2014, **392**, 45-50.
- 35 G. F. Wang, W. P. Qin, L. L. Wang, G. D. Wei, P. F. Zhu and R. J. Kim, *Opt. Express*, 2008, **16**, 11907-11914.
- 36 E. M. Chan, G. Han, J. D. Goldberg, D. J. Gargas, A. D. Ostrowski, P. J. Schuck, B. E. Cohen and D. J. Milliron, *Nano Lett.*, 2012, **12**, 3839-3845.